

UC Berkeley

UC Berkeley Previously Published Works

Title

Influence of Mesoscale Interactions on Proton, Water, and Electrokinetic Transport in Solvent-Filled Membranes: Theory and Simulation

Permalink

<https://escholarship.org/uc/item/46t820h9>

Journal

Langmuir, 38(34)

ISSN

0743-7463

Authors

Crothers, Andrew R
Kusoglu, Ahmet
Radke, Clayton J
[et al.](#)

Publication Date

2022-08-30

DOI

10.1021/acs.langmuir.2c00706

Peer reviewed

The Influence of Mesoscale Interactions on Proton, Water, and Electrokinetic Transport in Solvent-Filled Membranes: Theory and Simulation

Andrew R. Crothers^{a,b}, Ahmet Kusoglu^b, Clayton J. Radke^{a,c}, Adam Z. Weber^{a,b*}

^aDepartment of Chemical and Biomolecular Engineering, University of California, Berkeley,

Berkeley, CA 94720 USA

^bEnergy Technologies Area, Lawrence Berkeley National Laboratory

Berkeley, CA 94720 USA

^cEarth and Environmental Sciences Area, Lawrence Berkeley National Laboratory

Berkeley, CA 94720 USA

(*) to whom correspondence should be addressed. E-mail: azweber@lbl.gov

Abstract

Transport of protons and water through water-filled, phase-separated cation-exchange membranes occurs through a network of interconnected nanoscale hydrophilic aqueous domains. This paper uses numerical simulations and theory to explore the role of the mesoscale network on water, proton, and electrokinetic transport in perfluorinated sulfonic-acid (PFSA) membranes, pertinent to electrochemical energy-conversion devices. Concentrated-solution theory describes microscale transport. Network simulations model mesoscale effects and ascertain macroscopic properties. An experimentally consistent 3D Voronoi network topology characterizes the interconnected channels in the membrane. Measured water, proton, and electrokinetic transport properties from literature validate calculations of macroscopic properties from network simulations and from effective-medium theory. The results demonstrate that the hydrophilic domain size affects the various microscale, domain-level transport modes dissimilarly, resulting in different distributions of microscale coefficients for each mode of transport. As a result, the network mediates transport of species non-uniformly with dissimilar calculated tortuosities for water, proton, and electrokinetic transport coefficients (i.e., 4.7, 3.0 and 6.1, respectively, at a water content of 8 H₂O per polymer charge equivalent). The dominant water transport pathways across the membrane are different than those taken by the proton cation. Finally, the distribution of transport properties across the network induces local electrokinetic flows that couple water and proton transport; specifically, local electrokinetic transport induces water chemical potential gradients that decrease macroscopic conductivity by up to a factor of 3. Macroscopic proton, water, and electrokinetic transport coefficients depend on the collective microscale transport properties of all modes of transport and their distribution across the hydrophilic domain network.

Introduction

Water-swollen, phase-separated ion-exchange membranes are vital to numerous energy-conversion devices, including fuel cells, electrolyzer, and water-purification technologies.¹⁻⁴ For these technologies, the quintessential membrane chemistries are perfluorinated-sulfonic-acids (PFSA) (such as Nafion).² Improving the performance of energy-conversion technologies requires optimizing membrane properties either by altered membrane chemistry or by operating in conditions that bypass limitations of current chemistries.⁵⁻⁸ Both strategies rely on a sophisticated understanding of the molecular underpinnings of membrane properties and how they scale to macroscopic observables.⁵⁻⁸

Research on PFSA membranes often seeks physical bases for the measured values of transport properties, such as conductivity and water permeability, in terms of the molecular interactions among species.^{1,2,9-20} To this end, a microscale description of transport in a single representative (e.g., average) water-filled domain accounting for molecular interactions provides a transport property L^i (superscript i denotes a microscale property).^{19,21-26} The microscale transport property is then upscaled to compare with measured macroscopic properties by considering (1) that L^i describes transport in a water-filled domain (interstitial properties), whereas the membrane as a whole contains a water volume fraction ϕ with the polymeric component of the membrane remaining inert to aqueous transport, thereby making its measured properties an average over water-filled and polymer regions (superficial properties), and (2) that

transport occurs across a network of connected channels forming meandering pathways characterized by a single tortuosity τ .²³ Classically, these two factors scale the microscale property L^i to a macroscopic, measurable property L according to^{23,27}

$$L = \frac{\phi}{\tau} L^i \quad \mathbf{1}$$

where τ is the membrane water-domain tortuosity.

In principle, tortuosity characterizes the transport path length and depends on the topology of the material (i.e., how the various sized domains connect) and the distribution of domain transport properties.^{23,28} Tortuosity quantifies how the mesoscale—a lengthscale over which nano-domains are connected and distributed—influences macroscopic properties. In practice, τ is often an adjustable parameter.²³ Equation 1 is the so-called capillary model for transport and is widely used to understand transport in membranes and porous media.^{12,14,18,22–25,27,29} It is, however, not well recognized that tortuosity also varies with the particular transport property under consideration.²³ For example, water does not necessarily take the same pathways across the membrane as protons do.³⁰ This work studies the application of the capillary model and the nature of τ and, consequently, the mesoscale in PFSA membranes in which proton and water transport occur simultaneously.

Phase-separated, water-filled proton-exchange membranes present complications for the capillary model because the presence of water and a mobile cation gives rise to multiple modes of transport.^{1,2,18,31} Proton electrochemical-potential gradients, $\nabla \mu_{+i}$, generate an ion flux, N_{+i} , (e.g., an electric field generates current). Likewise, water chemical-potential gradients, $\nabla \mu_0$, induce a water flux, N_0 , (i.e., water diffusion or permeation). Because the (electro)chemical potential depends on pressure, a pressure gradient also drives mass transport.³² Additionally,

transport driving forces are coupled by electrokinetic phenomena such that ion electrochemical-potential gradients initiate a water flux (i.e., electroosmosis) and water chemical-potential gradients initiate an ion flux (i.e., streaming current).^{6,33} See Table 6 in Ref ².

Transport in such systems is mathematically described by non-equilibrium thermodynamics of concentrated solutions. For a system consisting of protons, water, and a membrane (with fixed anionic charges and no aqueous-phase free anions), the governing flux equations are^{27,33,34}

$$N_{+\dot{i}} = -L_{++\dot{i}} \nabla \mu_{+\dot{i}} - L_{+0} \nabla \mu_{0\dot{i}} \quad 2$$

and

$$N_{0\dot{i}} = -L_{0+\dot{i}} \nabla \mu_{+\dot{i}} - L_{00} \nabla \mu_{0\dot{i}} \quad 3$$

where L_{00} is the transport coefficient relating a flux of water to its chemical-potential gradient (proportional to water permeance), $L_{++\dot{i}}$ is the transport coefficient relating a flux of protons to its electrochemical-potential gradient (proportional to ionic conductivity), and L_{+0} is the electrokinetic transport coefficient relating the flux of protons to a water chemical-potential gradient (it should be noted that in some literature^{21,35} the transport coefficient L_{ij} is written as $c_i c_j L_{ij}$). This different formulation is convenient when relating to Stefan-Maxwell concentrated-solution formalism Onsager's reciprocal relationship dictates that $L_{+0} = L_{0+\dot{i}}$.^{34,35} In networks of inter-connected channels, the presence of coupling between transport modes makes effective transport properties challenging to rationalize in terms of microscale properties and simple upscaling.¹⁹ This paper explores how the capillary model represents these multiple modes of transport in proton-exchange membranes.

We build on previous literature on the effect of transport couplings in network structures transporting gas and electrokinetic phenomena in porous media.^{36,37} We explore these coupling relationships in the context of water-filled, phase-separated, cation-exchange membranes, expanding on prior network simulations of this material^{38–42} and experimental investigations.^{9,20} In particular, we study PFSA membranes because they are an essential component of energy-conversion applications and are widely characterized experimentally, allowing for model validation.²

PFSA membranes are nanophase separated with water-filled domains exhibiting sizes on the order of nanometers.^{1,2,43} The hydrophilic channels of PFSA membranes contain water and cations with negatively charged sulfonate (SO_3^-) groups imbedded in the channel walls that consist of the hydrophobic units of the polymer.^{1,2,43} This study considers Nafion PFSA membranes exchanged with protons. The equivalent weight (EW) of the membrane is the average mass of polymer per mole of sulfonate groups. For the Nafion membrane in this study, EW is 1020 g mol^{-1} (based on manufacture-reported titration and lower than the nominal 1100 g mol^{-1} cited in some literature).^{2,44} The water content of the membrane is quantified by λ , the molecules of water per sulfonate group and spans from ~ 0 when fully dried to ~ 22 when fully hydrated in liquid water, with the water activity of the environment controlling the average hydration level of the material.² The sizes of the hydrophilic domains or “channels” is widely distributed.^{2,43,45,46} PFSA materials are unlike classic porous media in that, in the dry state, the hydrophilic channels collapse and are not filled with gas or vapor.² The concept of the approach and inherent multiscale architecture are shown in Figure 1.

This paper is outlined as follows. First, we illustrate a pedagogical model of transport to show why transport coupling fundamentally alters the nature of tortuosity. We then turn to

realistic models of PFSA membranes by outlining a microscale description for the transport coefficients L_{ij}^c in a single water-filled domain of a PFSA membrane as a function of water content and domain size (see Figure 1). The microscale model provides the transport coefficients of individual segments of the mesoscale-network simulations of PFSA membranes using a physically consistent network topology (represented by a 3D Voronoi tessellation, as shown in Figure 1). Domain-size distributions informed by structural characterization. Network nodes exhibit no transport resistance. Effective-medium theory rationalizes the findings of these simulations. The network simulations and effective-medium theory predict the macroscopic transport properties L_{ij} . Measured transport properties from literature validate the model predictions. Finally, we examine the implications of our work and the nature of the capillary model and tortuosity in PFSA materials.

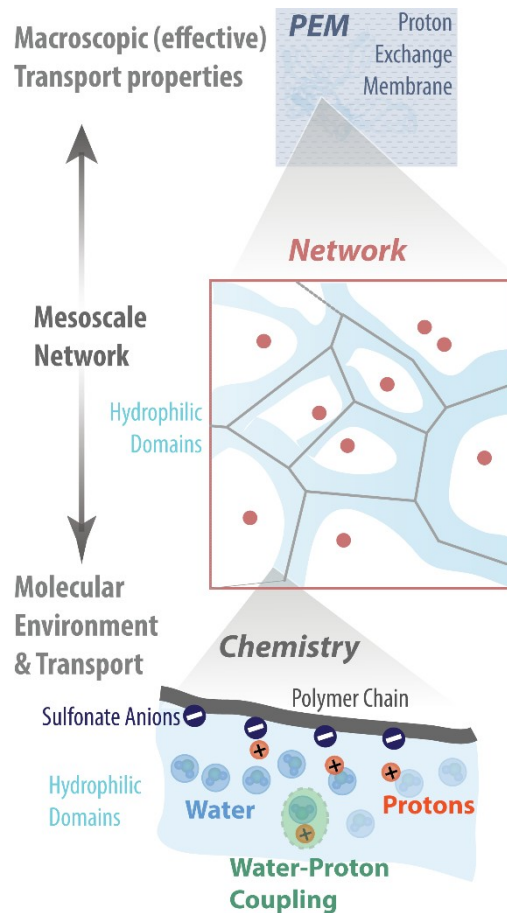


Figure 1. Multiscale structure of transport in the PFSA membrane going from locally flat channels to arranged multiscale network where the water domains are represented as the line interconnections in a 3-D Voronoi tessellation) to macroscale observables.

Results and Discussion

Pedagogical model

To illustrate the effect of domain-size distribution and transport coupling, consider the tortuosity of a simple network consisting of two channels a and b connected in series with the same cross-sectional area and length with different transport properties L^{i_a} and L^{i_b} for either water or protons. (We consider realistic networks with a branching topology in the next section.) Without transport coupling, Section A in the Supporting Information (SI) shows that the tortuosity of this network is

$$\tau = \frac{\phi L^i}{L} = \frac{(L^i)^2}{L^{i,a} L^{i,b}} \quad 4$$

where L is the effective transport property of the network and L^i is the arithmetic mean of $L^{i,a}$ and $L^{i,b}$. Tortuosity is unity when the transport properties of the segments are equal and $\tau > 1$ when transport properties are unequal. Equation 4 shows that if two modes of transport have different distributions of transport properties, the tortuosity of each mode is also different.

Now consider the role of transport coupling. For the same network with different conductive transport properties $L_{++i^a i}$ and $L_{++i^b i}$ with arithmetic mean $L_{++i^i i}$ and uniform water and electrokinetic transport coefficients L_{00}^i and $L_{0+ i^i i}$ respectively, the proton transport-coefficient (conductivity) tortuosity is, as section A in SI shows,

$$\tau_{++i} = \phi \frac{L_{++i^i i}}{L_{++i^a i} L_{++i^b i}} \quad 5$$

Equation 5 reduces to Equation 4 when there is no transport coupling ($L_{0+ i^i i} = 0$). Like the case of uncoupled transport (Equation 4), in coupled transport $\tau_{++i} = 1$ when the transport channels have the same transport properties. However, when channels do not have the same proton transport coefficient, transport coefficients for water transport and electrokinetics influence the tortuosity of the proton transport coefficient. This phenomenon arises because the difference between $L_{++i^a i}$ and $L_{++i^b i}$ induces an electrokinetic water chemical-potential gradient that drives additional proton flux. Even when there is no net water chemical-potential difference across both segments, there is a chemical-potential difference across the individual segment. It is, therefore, impossible to describe completely the effective ionic transport coefficient of this system without accounting for the water transport and electrokinetic properties. This is allowed because for a network consisting of two perfectly uniform channels in parallel, transport coupling does not impact tortuosity because there are no induced internal gradients. As such, transport coupling's influence

on tortuosity requires in-series transport, which is the case for most real-world network topologies including PFSA membranes. Surprisingly, in the limiting case that the water transport coefficient is zero, $L_{00}^{\dot{\zeta}}=0$, the tortuosity for proton transport is unity no matter the value of the proton transport coefficients. This result is starkly different than that of uncoupled transport (Equation 4). The simple model of two channels in series illustrates that coupling between water and ion transport mediates macroscopic transport properties at the mesoscale. The remainder of this paper explores this phenomenon when considering actual membrane systems that contain numerous connected channels with a heterogeneous size distribution and realistic microscale transport coefficients.

Microscale Transport Description

Microscale transport properties $L_{ij}^{\dot{\zeta}}$ are calculated by accounting for binary frictional interactions between cations, water, and the membrane using the Stefan-Maxwell formalism.^{21,35} As outlined in prior work,²¹ in a cation-exchange membrane with polymer (denoted M), water (denoted 0), and a proton (denoted $+\dot{\zeta}$), nonequilibrium thermodynamics dictates that the (electro)chemical-potential gradient drives mass transport. According to the Gibbs-Duhem relation, only two of these three electrochemical potential are independent.³⁵ In the Stefan-Maxwell formalism, the isothermal driving force is balanced by frictional drag interactions between species i and j and is proportional to their difference in species velocities, $v_i^{\dot{\zeta}}$ and $v_j^{\dot{\zeta}}$, multiplied by a friction coefficient $K_{ij}^{\dot{\zeta}}$.^{21,33}

$$c_{+\dot{\zeta}} \nabla \mu_{+\dot{\zeta}} = K_{+\dot{\zeta}0}^{\dot{\zeta}} v_0^{\dot{\zeta}} - K_{0+\dot{\zeta}}^{\dot{\zeta}} v_{+\dot{\zeta}}^{\dot{\zeta}}$$

$$c_0 \nabla \mu_0 = K_{0+\dot{\zeta}}^{\dot{\zeta}} v_{+\dot{\zeta}}^{\dot{\zeta}} - K_{+\dot{\zeta}0}^{\dot{\zeta}} v_0^{\dot{\zeta}}$$

6

where $c_i^{\dot{i}}$ is the concentration of species i . The assumption of local equilibrium underlies this formalism. As such, there is no superscript \dot{i} on the (electro)chemical potentials because they are the same at the microscale and macroscale. The membrane provides the reference velocity, $v_M^{\dot{i}}=0$, because the membrane is typically fixed (relative to the laboratory frame of reference). Equations and emerge after solving Equations for $v_0^{\dot{i}}$ and $v_{+\dot{i}\dot{i}}$ and by noting that flux is proportional to the species velocity ($N_i^{\dot{i}}=c_i^{\dot{i}}v_i^{\dot{i}}$). To specify $K_{ij}^{\dot{i}}$, we use the microcontinuum model, described previously,²¹ with the modifications detailed in section B of the SI. A brief summary is included here.

Charge transport in acidic solutions occurs, in part, through protons transporting via hopping along hydrogen-bond networks (i.e. the Grotthuss mechanism).^{1,2,8,47-53} The molecular nature of this transport in PFSA membranes and water more generally has been extensively studied but remains controversial.^{2,8,47-53} This paper does not address this topic explicitly, rather we treat water/cation friction coefficients as equivalent to those of a bulk-aqueous-electrolyte at an equivalent proton concentration. The short-range water/cation interactions justify the implicit assumption that the channel walls do not materially alter interactions between mobile species in solution.⁵¹ Literature shows that proton/water friction in bulk solution exhibits low friction at high water contents (i.e., high diffusion coefficient at low proton concentrations) but a high friction coefficient at low water contents (low diffusion coefficient at high proton concentrations), as Figure S2 in SI shows.^{1,54,55} The strong dependence on water content is due to a transition from protons transporting via hopping to vehicular transport at low water contents as water becomes bound up in proton's solvation shell and disrupts hydrogen bonding networks.^{1,55}

A classic electrokinetic treatment specifies the water/membrane and mobile cation/membrane friction coefficients.²¹ Specifically, the Navier-Stokes equation describes an aqueous solution flowing through charged channels with no-slip boundary conditions.^{21,35} Our model uses the linearized Poisson-Boltzmann equation to specify the distribution of cations throughout the channel.^{21,35} The solution to this system of equations provides the interspecies friction coefficients as a function of membrane water content, λ , and domain size.

Chemical-reaction equilibrium specifies the fraction of protons immobilized due to desolvation and pairing with the fixed, anionic sulfonate groups as a function of water content. The ion-pairing equilibrium constant is obtained by fitting the calculated fraction of cations paired with sulfonate groups to *ab-initio* molecular-dynamics simulations of PFSA (see Figure S1).⁵⁶

In quantifying water/membrane and mobile cation/membrane friction, the hydrophilic PFSA domains are considered locally flat with appended sulfonate groups distributed along the domain/polymer interface.⁴³ For a flat-channel geometry, the channel height of a single domain H^i is a function of water content λ and the local channel interfacial area per sulfonate charge $A_{SO_3}^i$

$$H^i = \frac{\dot{V}_0 \lambda}{N_A A_{SO_3}^i} \quad 7$$

where the volume of cations is negligible, \dot{V}_0 is the partial molar volume of water (approximated as equal to the molar volume of pure water), and N_A is Avogadro's number. The mean average height of all the channels in the membrane is H^{ave} . Small-angle X-ray scattering (SAXS) of Nafion under different hydration conditions provides the mean channel height as a function of

water content. The linear relationship between H^{ave} and water content, λ , from Equation 7 specifies the surface area per sulfonate group as $A_{SO_3}^{ave}$ (for Nafion, $A_{SO_3}^{ave} = 0.23 \text{ nm}^2$).² We consider the sulfonate groups arrayed on a square-lattice at the hydrophilic/hydrophobic domain interface, giving a spacing between sulfonate groups as $l_{SO_3}^i = \sqrt{A_{SO_3}^i}$. The distance between sulfonate groups of the average-height-domain is denoted $l_{SO_3}^{ave}$ (because the mean and square-root functions are not permutable, the mean of $l_{SO_3}^i$ is not equivalent to $l_{SO_3}^{ave}$).

Molecular-scale variations in the equivalent weight and the semi-crystallized nature of PFSA create a wide distribution of sulfonate groups spacing, $l_{SO_3}^i$.^{2,43,45,46} A result of this polydispersity is that a PFSA membrane contains a wide distribution in channel heights.

Figure 2 shows calculated (a) microscale proton transport coefficient L_{++i}^i , (b) electrokinetic transport coefficient L_{0+i}^i , (c) and water transport coefficient L_{00}^i , as a function of water content λ and the ratio of channel height to average channel height H^i/H^{ave} (see section B in SI for calculation details). Up to moderate water contents ($\lambda \sim 10$), the proton transport coefficient L_{++i}^i increases with water content as the protons solvate, encounter less hydrodynamic resistance with the channel walls, and increasingly transport via the hopping mechanism. At high water contents, increasing membrane water content dilutes protons and reduces its transport coefficient.

For small channels (small H^i/H^{ave}), increasing channel height decreases hydrodynamic resistance with the walls, thereby increasing the cation transport coefficient L_{++i}^i . However, the dependence of L_{++i}^i on H^i reverses for thick channels. At high H^i/H^{ave} , the cations are confined to the walls due to electrostatic attraction to the closely packed sulfonate groups. Increasing

channel height further confines protons near to the walls, increasing hydrodynamic resistance and decreasing proton transport.

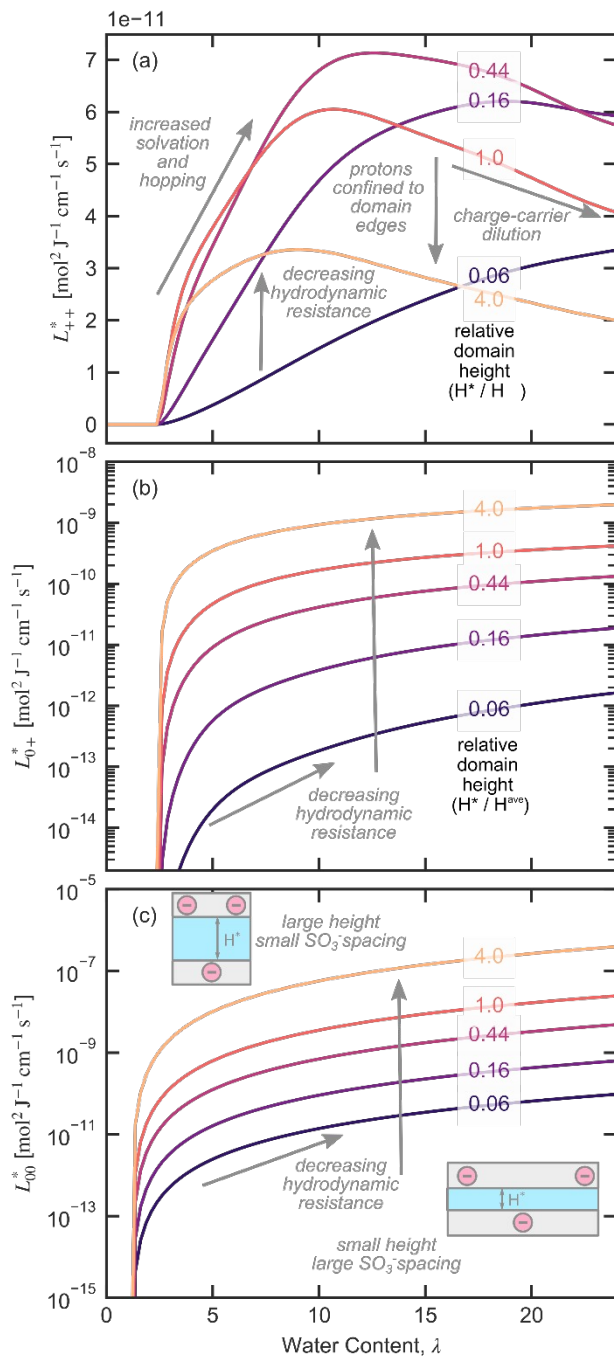


Figure 2. Microscale channel transport coefficients for (a) proton transport L_{++}^* , (b) electrokinetic transport L_{0+}^* and (c) water transport L_{00}^* as a function of water content λ for different channel heights relative to the average height, H^i / H^{ave} . Section B in SI details the calculations.

Hydrodynamic interactions with the channel walls govern the electrokinetic transport

coefficient L_{0+}^i and the water transport coefficient L_{00}^i . As water content and channel height increase, the electrokinetic and water transport coefficients increase monotonically.

Upscaling and the Macroscopic Transport Description

An important finding from Figure 2 is that the values of L_{ij}^i transport coefficients have different dependences on different domain sizes at the same water content. As we show later, this finding leads to different tortuosities and different pathways for water and protons to traverse the membrane. The following subsections first discuss the distribution of channel heights in the membrane. Then, we outline Voronoi tessellation resistor-network simulations, where each segment is parameterized by the microscale model, to determine effective, macroscale transport properties. Effective-medium theory provides a mean-field approach to generalize the findings of simulations.

Microscale Channel-Size Distribution

The wide distribution of channel heights as seen in Figure 2 creates a distribution of transport properties. The thickest channels of a membrane for a fixed water content correspond to channels with sulfonate groups packed to their distance of closest approach on the top and bottom domain walls, $l_{SO_3}^i = l_{SO_3}^{DCA}$. The distance of closest approach between sulfonate groups is 0.4 nm,⁵⁷ but because sulfonate groups are present on both the top and bottom walls of the domain there are twice as many sulfonate groups per interfacial area making $l_{SO_3}^{DCA}$ half this distance, or 0.2 nm. To calculate the domain-size distribution, we quantify the probability that a domain has a given spacing between sulfonate groups beyond the distance of closest approach

$l_{SO_3}^i - l_{SO_3}^{DCA}$ with⁵⁸

$$PDF(l_{SO_3}^i - l_{SO_3}^{DCA}) = \frac{1}{\left(\frac{l_{SO_3}^i - l_{SO_3}^{DCA}}{1 [m]}\right) \sigma_{l_{SO_3}} \sqrt{2\pi}} \exp\left(-\frac{\left[\ln\left(\frac{l_{SO_3}^i - l_{SO_3}^{DCA}}{1 [m]}\right) - \mu_{l_{SO_3}}\right]^2}{2 \sigma_{l_{SO_3}}^2}\right)$$

where PDF is a log-normal probability distribution function of $l_{SO_3}^i - l_{SO_3}^{DCA}$ in units of meters, and $\sigma_{l_{SO_3}}$ and $\mu_{l_{SO_3}}$ are parameters of the distribution. We choose the log-normal distribution because polymer chain lengths are known to follow this distribution.⁵⁹ The factor of 1 m makes the argument of Equation 8 non-dimensional. Equations 7 and 8 and the microscale properties in Section B in SI provide the distribution of domain sizes and transport properties. These distributions parameterize the network simulations that are discussed in the next section. We fit the network simulations of macroscopic proton, water, and electrokinetic transport properties with measured values by adjusting $\sigma_{l_{SO_3}}$, with a resultant best-fit value of 1.52. Integration of the product of Equation 8 and $1/(l_{SO_3}^i)^2$ specifies the mean of inverse area per sulfate group, $1/A_{SO_3}^{ave}$.⁵⁸ To ensure that the distribution of $l_{SO_3}^i$ with a given $\sigma_{l_{SO_3}}$ is consistent the experimental $A_{SO_3}^{ave}$, we numerically solve for $\mu_{l_{SO_3}}$ ($= -21.36$) using Brent's method⁶⁰ so that the mean of $1/(l_{SO_3}^i)^2$ is equal to the SAXS measurements of $1/A_{SO_3}^{ave}$.²

Figure 3a shows the calculated PDF of channel height $PDF(H^i)$ for $\lambda=20$ using random variants of $l_{SO_3}^i$ sampled using Equation 8 and from calculation of height using Equation 7. The probability distribution extracted from transmission electron microscopy (TEM) of a hydrated Nafion film ($\lambda=20$) provides comparison.^{45,46} The model-fit and TEM distribution are similar although differences exist. The proposed model-fit distribution is wider and slowly decreases with increasing H^i whereas the distribution from TEM is narrower and peaks around 0.75 nm.

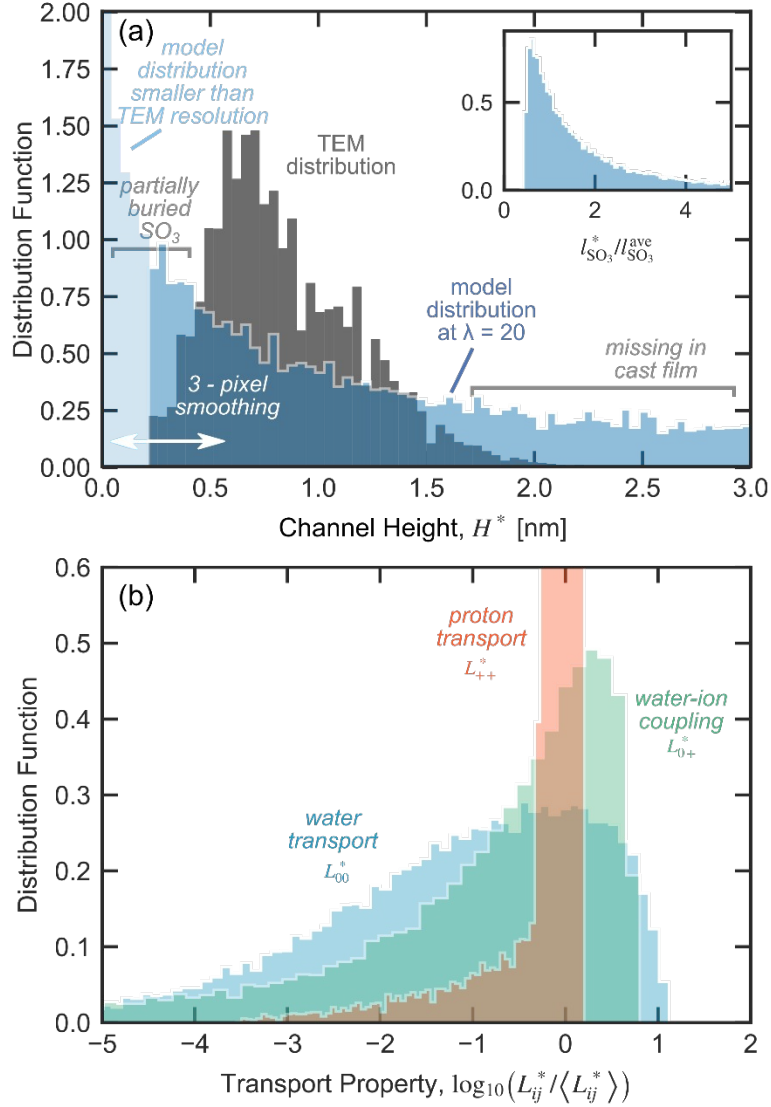


Figure 3. Probability-distribution function of channel heights from (a) transmission electron microscopy^{45,46} and from using 20,000 random variants of $l_{SO_3}^*$ sampled in Equation 8 and calculating channel height in Equation 7 each at $\lambda=20$ and (b) the probability-distribution function of proton, water, and electrokinetic transport coefficients corresponding to the channel-size distribution as detailed in Section B of SI. Insert in (a) shows random variants of $l_{SO_3}^*$ normalized to $l_{SO_3}^{ave}$ sampled from Equation 8.

Three limitations of TEM analysis and sample preparation help rationalize the discrepancies between the model-fit and TEM distributions for small channels sizes. First, TEM does not capture very small channels because they are below the limit of experimental detectability (0.224 nm).⁴⁵ Second, to identify the interface between hydrophilic and hydrophobic channels and to reduce noise, a 3-voxel median filter was applied to the TEM image.⁴⁶ The de-

noising process means that some small channels (up to 3-voxel across a dimension, or 0.672 nm) do not appear in the TEM distribution. These small channels consist of sulfonate groups that are partially buried in the hydrophobic matrix and allow only a small amount of water or ions to move through them as shown by recent S-edge SAXS.^{61,62} Further, a wide distribution of $l_{SO_3}^i$ is consistent with the measured wide distribution of EWs for the same membrane chemistry due to batch-to-batch variability⁶³ (see Figure 3a inset showing probability distribution function of $l_{SO_3}^i/l_{SO_3}^{ave}$ where the spacing between sulfonate groups scales with the local EW of membrane surrounding the channel). Finally, TEM requires 100-nm thick cast-thin films, whereas the model distribution is fit to experiments of bulk membranes that have undergone various pretreatment or processing conditions.^{2,45} As a result, the model distribution contains large channels that could have resulted from sample preparation of the membranes that was not present in the thin-film TEM sample.

Figure 3b shows the probability distribution of the proton, water, and electrokinetic transport coefficients at $\lambda=20$ shown in Figure 2 using the distribution in Figure 3a. Water transport properties vary by an order of magnitude with channel height, whereas the proton transport coefficient is relatively independent of channel height (Figure 2). As a result, the water and electrokinetic transport coefficients have a wide distribution, but the proton transport coefficient distribution is narrow. Each transport property has a different distribution because they depend differently on channel size (see Figure 2).

Resistor-Network Simulations

A 3D network of interconnected channels simulates the PFSA-membrane effective transport properties. Segments of the network represent water-filled channels and zero-volume

nodes represent connections between channels. We use a Voronoi tessellation to represent the topology of PFSA membranes, where tessellation edges represent water-filled domains (see Figure S3). A Voronoi tessellation is a realistic representation of the PFSA microstructure, with a coordination number of 3 (average number of segments connected to a node) and with slit channels anisotropically oriented locally but, on average, isotropic as depicted in Figure 1.^{2,46} Section C in SI details network construction that gives n_S segments connecting n_N nodes distributed across a 3D cube of dimensions L^{net} .

The walls of each channel have a sulfonate spacing $l_{SO_3}^c$, sampled from the probability distribution in Equation 8, giving each channel a height at a specific water content (see Equation 7) with corresponding proton, water, and electrokinetic transport properties, as Figure 2 shows (see Section B in SI for calculation details). Let $Q_i^{a,\beta}$ be the net molar flow rate of water or protons into each node a from connecting node β . At steady state, the net (scalar) flow into or out of each non-boundary node a , from all connecting nodes β is zero, or

$$-\sum_{\beta} Q_i^{a,\beta} = 0 \quad 9$$

where the molar flow is the product of the interstitial molar flux and the cross-sectional area of the segment (i.e. product of channel height $H^{a,\beta}$ and width, $W^{a,\beta}$),

$$Q_i^{a,\beta} = N_i^{a,\beta} H^{a,\beta} W^{a,\beta}. \quad 10$$

The width of each channel is set equal to W^{ave} .

The interstitial flux through a segment connecting nodes a from β , $N_i^{a,\beta}$, obeys the flux Equations 2 and 3 written for each segment

$$N_{+c}^{a,\beta} = -L_{++}^{a,\beta} \frac{\mu_{+c}^a - \mu_{+c}^\beta}{L_{++}^{a,\beta}} - L_{-c}^{a,\beta} \frac{d^a \mu_{-c}^a}{L_{-c}^{a,\beta} d^a c} \quad 11$$

and

$$N_0^{\alpha,\beta} = -L_{0+\hat{i}}^{\alpha,\beta} \frac{\Delta^{\alpha,\beta} \mu_{\hat{i}}}{A^{\alpha,\beta}} - L_{00}^{\alpha,\beta} \frac{\Delta^{\alpha,\beta} \mu_0}{A^{\alpha,\beta} \hat{i}}$$

where $L_{ij}^{\alpha,\beta}$ is the transport coefficient $L_{ij}^{\hat{i}}$ of the segment connecting α and β , $A^{\alpha,\beta}$ is the length of the channel parallel to the direction of transport, and $\Delta^{\alpha,\beta} \mu_i$ is the change of electrochemical potential of protons or chemical potential of water from node β to α , $\Delta^{\alpha,\beta} \mu_i = \mu_i^\alpha - \mu_i^\beta$. Equations 11 and 12 assume that transport coefficient $L_{ij}^{\alpha,\beta}$ is independent of μ_i between nodes α and β . This is a good assumption if $\Delta^{\alpha,\beta} \mu_i$ is small. Application of a small (electro)chemical-potential change across the network satisfies this requirement. Said alternatively, macroscopic gradients necessarily cause small microscale water-content changes.

To specify the effective network transport coefficients (i.e., the macroscopic transport properties), the algorithm sets the (electro)chemical potential of the nodes on the left boundary ($x=0$) as the zero reference (i.e., $\mu_i=0$) for both species. On the right boundary nodes, a small potential drop relative to the left boundary, $\Delta^{net} \mu_i$ is set for both species in turn. As Section D in SI details, solution of Equation 9 for each internal node (i.e. non-boundary node) along with Equations 11 and 12 for each segment specifies the water and proton flow through the nodes and segments. We treat the water content as constant across the membrane, corresponding to a small $\Delta^{net} \mu_i$. Therefore, $L_{ij}^{\hat{i}}$ is independent of $\Delta^{net} \mu_i$, and $Q_i^{\hat{i}}$ is linear with $\Delta^{net} \mu_i$. If the change in chemical potential is small across the representative elementary volume of the system (shown subsequently to have dimensions of ~ 60 nm), concentration-dependent transport properties will change negligibly and there will be a linear relationship between flux and driving force at this scale. For example, a 10 μm thick membrane equilibrated with liquid water on one side and dry air on the other side will only have a 0.13 change in λ over 60 nm (using water content from Ref

2), yielding negligible transport properties changes across this distance. Overall nonlinear behavior for the transport phenomena is still witnessed at the aggregated macroscopic level.

Figure 4 shows calculated flows of protons (a)-(c) and induced water (electrokinetic flow) (d)-(f) under a proton electrochemical-potential difference across the network and water flow (g)-(i) with a water chemical-potential drop. Each line is a network channel with line thickness scaled proportionally to its height. Circle sizes scale proportionally to the species flow through the channel (see Equation 10). Panels (a), (d), and (g) show flows at low membrane hydration, panels (b), (e), and (h) are at moderate hydration, and panels (c), (f), and (i) illustrate fluxes at high hydration. To make qualitative inferences possible, visualizations in Figure 4 are in 2D, whereas network simulations are 3D for reporting quantitative properties and comparison to experimental data.

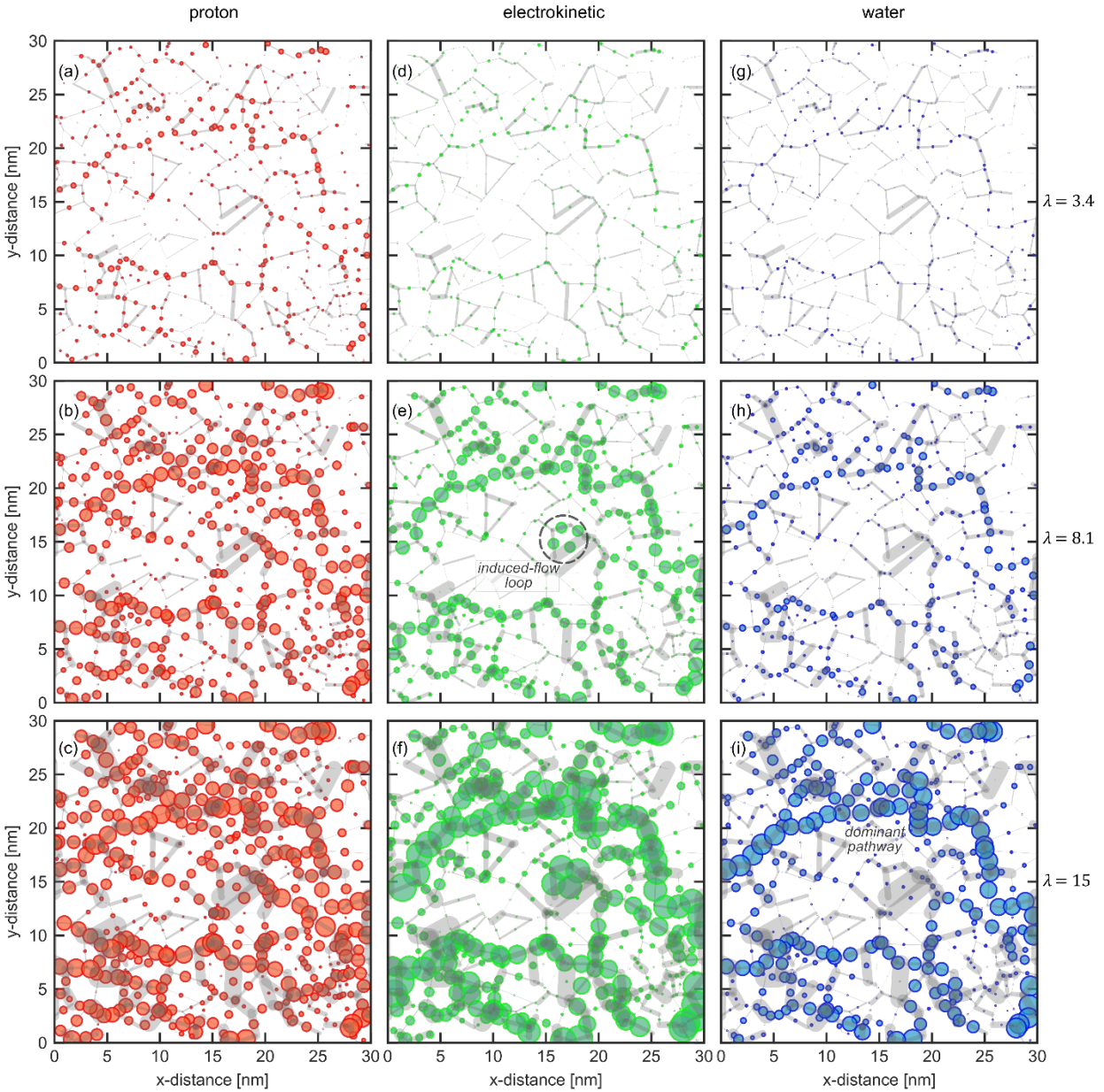


Figure 4. Network simulation flows of (a)-(c) protons and (d)-(f) water (electrokinetic) under a proton electrochemical-potential difference, and (g)-(i) with a water chemical-potential drop. Lines are network channels scaled proportionally with the channel height. Circled areas are scaled proportional to species flow. (a), (d), and (g) show flows at a $\lambda=3.4$, (b), (e), and (h) are at $\lambda=8.1$, and (g), (f), and (i) illustrate fluxes at $\lambda=15$. Note the induced-flow loop (e).

Figure 4 demonstrates that flows increase with increasing water content for the same $\Delta^{net} \mu_i$ as the channels expand and transport properties generally increase. However, for each membrane water content different modes of transport take considerably different pathways across the membrane. Due to the narrow distribution of proton transport properties (see Figure 3),

protons transport across most segments. Conversely, as Figure 4 reveals, water and electrokinetic transport properties are widely distributed giving a strong preference for some pathways over others.

All else being equal, species transport pathways favor channels with large heights. As Figure 4 shows, however, this criterion is insufficient to predict high flows through a network. Specifically, transport through a channel also depends on the (electro)chemical-potential drop across it that, in turn, is a function of the collective transport properties of nearby channels. The distribution of transport properties induces local (electro)chemical-potential gradients. Figure S4 in SI shows calculated proton electrochemical-potential (a) and water chemical potential (b) of each node under a proton electrochemical-potential difference across the network (see Section D in SI) as a function of position at $\lambda=15$. The proton electrochemical potential declines across the network but does not decrease uniformly between the left and right sides of the network. Even with no macroscopic water chemical-potential drop (i.e., $\Delta^{net} \mu_0=0$), the distribution of transport properties generates local water chemical-potential gradients. Local gradients induce electrokinetic flow loops that pump flow in circles, as Figure 4e notes, and which have been observed in saturated porous media under electric fields.³⁶

To understand how mesoscale flows dictate macroscopic properties, we sum the flows passing through the network and normalize by the total cross-sectional area of the network (including both hydrophilic and hydrophobic phase-separated areas) to specify the macroscopic (superficial) fluxes in the network of species i , N_i^{net} (see Section D in SI for details). Macroscopic effective network transport coefficients are related to network fluxes, length of the network L^{net} , and applied potential. When $\Delta^{net} \mu_0=0$,

$$L_{++\dot{c}}^{net} = -N_{++\dot{c}} \frac{W^{net}}{\Delta^{net} \mu_{++\dot{c}}} \dot{c} \quad 13$$

and

$$L_{0+\dot{c}}^{net} = -N_{0+\dot{c}} \frac{W^{net}}{\Delta^{net} \mu_{0+\dot{c}}} \dot{c} \quad 14$$

and when $\Delta^{net} \mu_{++\dot{c}} = 0$

$$L_{00}^{net} = -N_{00} \frac{W^{net}}{\Delta^{net} \mu_0}. \quad 15$$

Network simulations obey Onsager's reciprocal relations such that $L_{0+\dot{c}} = L_{+0\dot{c}}$.

The transport coefficients L_{ij} are rarely measured directly experimentally.^{5,33} Rather, experiments characterize slightly different sets of transport properties that are measurable under well-defined conditions. Under an applied electric field with constant water chemical potential, the conductivity κ and electroosmotic coefficient ξ characterize ion and water transport, respectively.^{5,6,33} The water transport coefficient α characterizes water transport across a membrane due to a water chemical-potential gradient in the absence of current. These transport coefficients relate to the L_{ij} coefficients according to³³

$$\kappa = L_{++\dot{c}F^2, \dot{c}} \quad 16$$

$$\xi = \frac{L_{0+\dot{c}}}{L_{++\dot{c}, \dot{c}}} \dot{c}$$

and

$$\alpha = L_{00} - \frac{L_{0+\dot{c}}^2}{L_{++\dot{c}, \dot{c}}}$$

We followed Weber and Newman⁶ to convert water-tracer diffusion coefficients measurements (i.e. from pulse-field-gradient nuclear magnetic resonance) to α and the procedure by Delacourt and Newman⁶⁴ to convert water-permeance measurements to α .

Figure 5 shows network-calculated transport properties (dashed line) and measured transport properties (symbols) of macroscopic (a) conductivity κ ^{65–75}, (b) electroosmotic coefficient ξ ^{5,69,76–79}, and (c) water transport coefficient α ^{9,71,80–85} as a function of water content λ . Calculations are the average of 5 randomly seeded 3D-network simulations with a characteristic system size, L^{net} , of 80 nm and from Equations 13 through 16 to obtain the transport coefficients. As we show later, an 80 nm network is sufficiently large for calculated transport properties of the network to correspond to macroscopic properties. We adjusted the sulfonate spacing distribution parameter σ_{SO_3} to fit these data sets, as noted above.

The Voronoi network simulations of conductivity agree with experiments up to high water contents ($\lambda \approx 17$). Macroscale conductivity increases monotonically with water content in contrast to domain-scale proton transport that displays non-monotonic behavior (see Figure 2). The difference in microscale and macroscale behavior arises from: (1) the definition of superficial macroscale transport that makes it scale with water volume fraction (see Equation), and (2) increasing water content decreases the tortuosity of proton transport across the membrane, thereby increasing conductivity.⁸⁶

The electrokinetic transport coefficient, ξ , increases monotonically with water content because higher water content increases L_{0+ii} faster than it does L_{++ii} . Figure 5 shows that ξ evidences a decreased slope at a water content of about 6. This regime change occurs because proton hopping increases at these water contents (see Figure 2B), making the increase of proton transport with water content greater than the increase of electrokinetic water transport with water content (i.e., $dL_{++ii}/d\lambda > dL_{0+ii}/d\lambda$). Our network simulations agree with experiments ξ over the entire range of hydration levels.

The water transport coefficient α increases monotonically with water content as expected from the microscale-transport coefficients in Figure 2. Again, network simulations agree with water transport coefficients measured by pulse-field gradient nuclear magnetic resonance and by hydraulic flow measurements.

Comparison to Effective-Medium Theory

For PFSA membranes, network simulations reveal that protons and water take different pathways across the membrane and that the distribution of channel transport coefficients induces local (electro)chemical-potential gradients. Effective medium theory (EMT) generalizes network simulations.⁸⁷ EMT, developed by Kirkpatrick, calculates effective transport coefficients of transport networks.⁸⁷ The theory considers a single segment with transport property L_{ij}^{ζ} interacting with an “effective medium” network with each segment having a transport property L_{ij}^{EMT} . For a network entirely consisting of segments with transport properties L_{ij}^{EMT} , an external field (i.e., an (electro)chemical-potential gradient) causes a uniform (electro)chemical-potential drop between parallel cross sections of the network normal to the direction of transport. The presence of L_{ij}^{ζ} causes an additional local field that decays over a large region of the network. For L_{ij}^{EMT} to represent accurately an actual network containing a distribution of segments with different transport properties L_{ij}^{ζ} , EMT requires that the internal fields induced by the presence of each segment sum to zero.

We adapt the method of Bonilla and Bhatia for multicomponent EMT, as detailed in Section E in SI and in Ref ⁸⁸. EMT accounts for the local proton electrochemical-potential gradients caused by variations in $L_{++\zeta\zeta}$ and the local water chemical-potential gradients induced

by variations in L_{00}^i . Multicomponent EMT also incorporates how electrokinetic coupling between water and protons transport link variations of L_{+0}^i and L_{00}^i to induced local proton electrochemical-potential gradients.

Solid lines in Figure 5 show (a) conductivity, (b) electroosmotic coefficient, and (c) water transport coefficient calculated using EMT (see Section E in SI). EMT shows very good agreement for conductivity and good agreement for electrokinetic and water transport coefficients. The slight disagreement between network simulations and EMT arises because we neglect the distribution of domain lengths when performing the EMT integration.

The success of multicomponent EMT in this case suggests a useful upscaling method for other microscale theories of membrane transport without requiring computationally intensive network simulations. However, EMT describes systems sufficiently large that the locally induced fields average out. As such, EMT cannot describe phenomena, such as induced-flow loops, that occur over shorter length scales for which locally induced fields cannot be averaged.

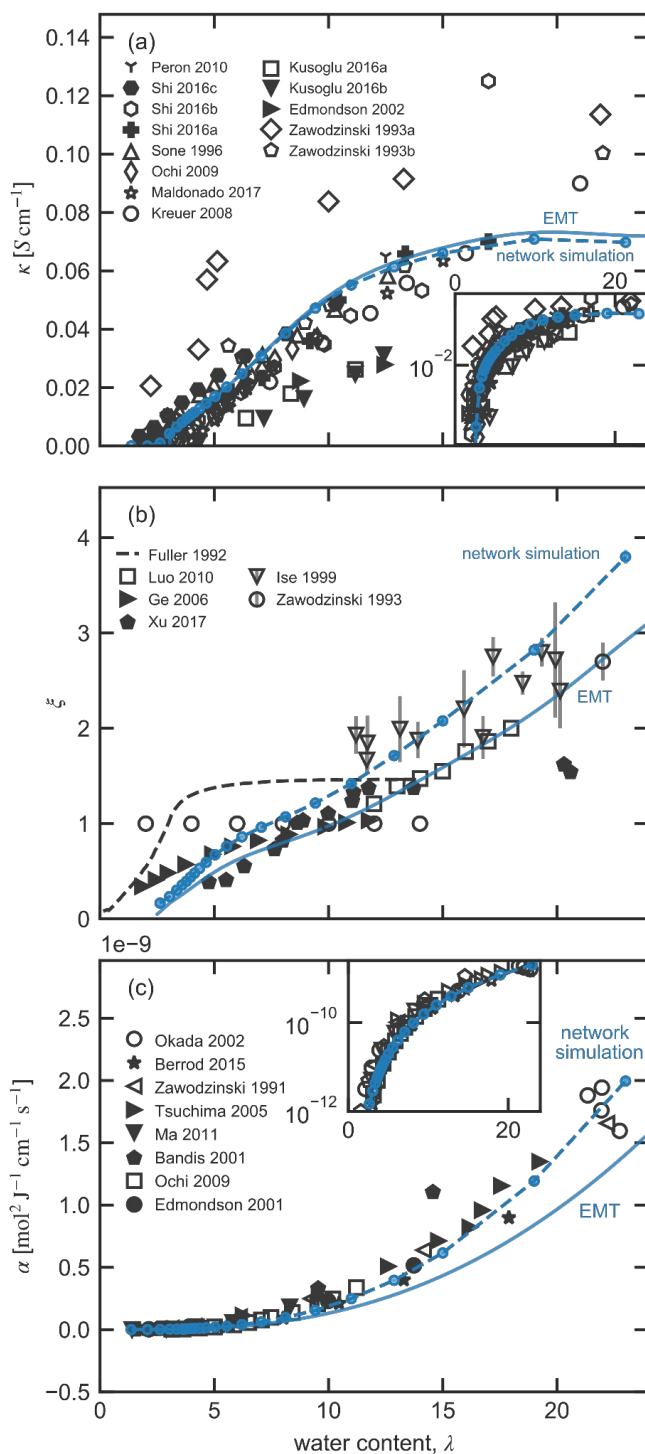


Figure 5. Experimental (symbols) and calculated (lines) (a) macroscopic conductivity κ (data from Refs ⁶⁵⁻⁷⁵), (b) electroosmotic coefficient ξ (data from Refs ^{5,69,76-79}). Black dashed line are an inferred measurement give in Ref. ⁵), and (c) water transport coefficient α (data from Refs ^{9,71,80-85}) from network simulations (dashed blue lines) and effective medium theory using Equation S20 in SI (solid blue lines) and measured coefficients from literature (symbols) as a function of water content λ for systems at temperatures between 22-30°C. Inserts show same plots on a \log_{10} y-axis scale. Open symbols are from data sets characterizing pretreated membranes and filled symbols are from data sets of membranes without pretreatment.

Effect of the Mesoscale on Transport

Tortuosity quantifies the impact of the mesoscale on transport. According to Equation 1, tortuosity is the ratio the effective macroscopic properties from the network simulations (see Figure 5) to the microscale transport properties of a representative channel with an average height H^{ave} (see Figure 2). Figure 6a shows the tortuosity τ_{ij} of transport coefficient L_{ij} as a function of water content. The tortuosity of each transport property is strikingly different. The tortuosity of proton transport decreases with water content, the tortuosity of water transport is constant for different water contents, and the tortuosity of electrokinetic transport increases with water content. For $\lambda > 3$, the tortuosity of proton transport is smallest, then water transport, and is largest for electrokinetic transport. The network visualization in Figure 4 corroborates this result: proton flux is more homogeneous with increasing water content, whereas electrokinetic fluxes are more widely distributed at higher hydration.

To understand the role of electrokinetic coupling on tortuosity, dashed lines in Figure 6a show the tortuosity of water and proton transport predicted from the network simulations with no electrokinetic coupling, i.e., with $L_{0+}^i = 0$. When electrokinetic coupling is present, locally induced water chemical potential gradients increase the path length of proton transport through the membrane. As a result, in the absence of electrokinetic coupling, proton transport tortuosity decreases. Upon setting $L_{00}^i = 0$, simulations reveal an even lower proton-transport tortuosity, as the dot-dashed line in Figure 6a shows. These results demonstrate that macroscopic transport coefficients are partially a function of the collective microscale proton, water, and electrokinetic transport properties and their domain distributions.

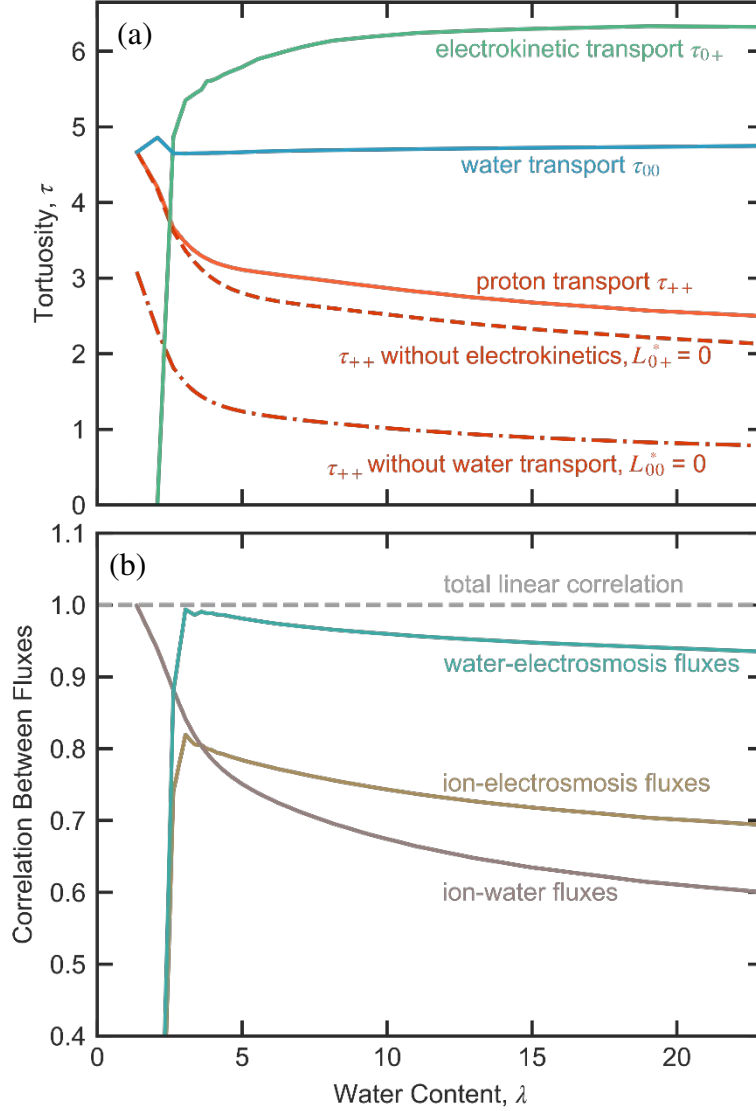


Figure 6. Tortuosity from network simulations at 80 nm and microscale theory (a) using Equation 1 for proton τ_{++} , water τ_{00} , and electro kinetic τ_{0+} transport coefficients and (b) correlation coefficient (1 = total linear correlation) between ion/water, ion/electrokinetic, and water/electrokinetic flows through segments in the 80-nm network simulations as a function of water content, λ . Dashed and dot-dashed lines in (a) show simulated network proton tortuosity, τ_{++} , for $L_{0+}^* = 0$ and for $L_{00}^* = 0$, respectively.

Figure 4 and Figure 6a clearly confirm that tortuosity, a crude measure of the mesoscale length of transport pathways, is different for each transport mode. To quantify the overlap between transport pathways of different transport modes, we calculate the correlation coefficient between water, proton, and electrokinetic flows through domain segments in the network

simulations.⁵⁸ A correlation coefficient of unity corresponds to complete positive linear correlation between flows of different transport modes (i.e., transport takes place in the same network segments). The coefficient is zero if there is no linear correlation between fluxes of different transport modes. Figure 6b plots the correlation coefficient of proton/water fluxes, proton/electrokinetic fluxes, and water/electrokinetic fluxes as a function of water content. The calculated correlation coefficients quantify what Figure 4 shows qualitatively, namely, water and electrokinetic flows transport through similar channels, but these channels are rather different from those taken for proton transport. Here again, these results arise from the different transport-property distributions.

Network simulations confirm the EMT description of “local” (electro)chemical-potential gradients developed because of the distribution of segment transport properties (see Figure 4). Local gradients influence the transport pathways and, in turn, affect the macroscopic transport coefficients. EMT does not quantify the distance over which gradients are important. To quantify this length scale, Figure 7 plots effective transport properties predicted from network simulation L_{++}^{net} (circles), L_{0+}^{net} (triangles), and L_{00}^{net} (squares) as a function of the characteristic network size at $\lambda=8.1$. Each point results from a network simulation with a different seed (i.e. different Voronoi tessellations and different random samplings of the segment sulfonate spacing from Equation 8). All transport properties are normalized to those simulated with 80-nm networks. All systems are periodic in the direction perpendicular to transport.

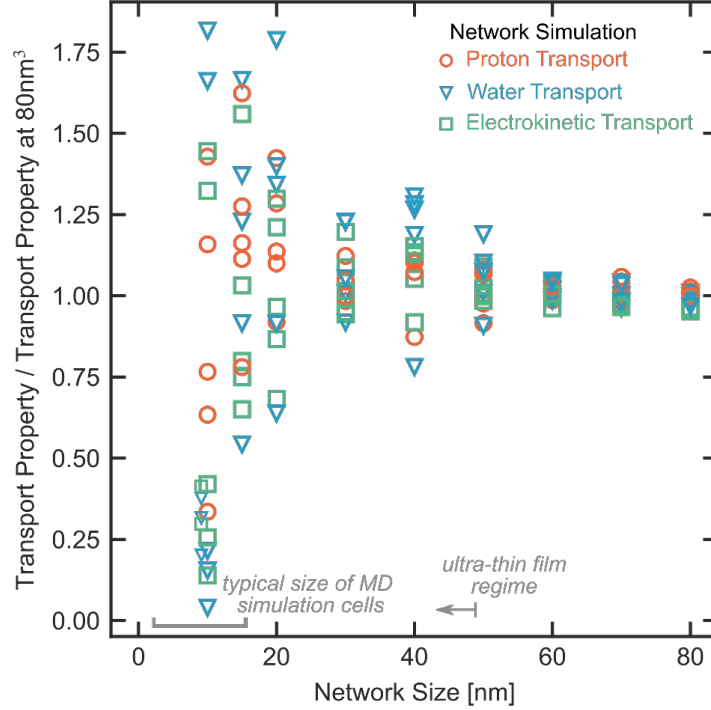


Figure 7. Network-simulated transport coefficients L_{++}^{net} (circles), L_{0+}^{net} (triangles), and L_{00}^{net} (squares) as a function of the network dimension at $\lambda=8.1$. Each point represents a random seeding. Transport properties are normalized by the mean of those simulated with 80-nm networks.

For small system sizes, different network realizations predict drastically different transport properties. Properties with a wider distribution of microscale transport properties (water and electrokinetic transport) vary more between different network configurations of the same network size. The representative volume element is the system size above which transport coefficients do not change and is, therefore, large enough to behave as a macroscopic system. For this system, the representative volume element has a characteristic dimension of around 60 nm. Variations in channel transport coefficients, L_{ij}^i , induce local (electro)chemical gradients on this scale.

For proton, water, and electrokinetic transport in PFSA, length scales between the microscale (~1 nm hydrophilic domains) and the macroscale (characterizable by a representative

elementary volume that has dimensions of 60 nm in this case) constitute the intermediate mesoscale. The lower and upper bounds of this length scale depend upon the size distribution of domains and upon the type of phenomena. For example, the representative elementary volume for mechanical properties or gas transport in PFSA membranes may be considerably different.

The representative volume in Figure 7 is much larger than the size most molecular simulations can achieve given the computation cost of simulating large systems (< 10 nm dimension cubes).^{47,48,57} This limitation could explain some of the differences between properties simulated with molecular dynamics and experiment. Moreover, the representative volume corresponds to the size below which PFSA thin films experimentally exhibit anomalous transport properties relative to a bulk system.^{2,66,89,90} Previous literature attributes this behavior to confinement of the polymer to the length scale of its persistence length.^{2,66,89,90} The results in Figure 7 show that anomalous thin-film transport behavior also take place on the same length scale as locally induced transport gradients.

Conclusions

This paper explores the nature of mesoscale transport in PFSA membranes including the role of electrokinetic coupling. We use a microscale concentrated-solution theory to calculate water, proton, and electrokinetic transport properties of single water-filled hydrophilic channels in PFSA membranes as a function of channel height and water content. The microscale model parameterizes resistor-network simulations with a realistic domain size distribution and Voronoi-network topologies that ascertain macroscopic transport coefficients. Using the variance of the domain-size distribution as the single adjustable parameter, we accurately predict measured membrane water, proton, and electrokinetic-transport properties. We use effective-medium

theory to rationalize how domain-scale variations of size and corresponding transport properties interact over the entire network to produce macroscopic properties.

Network simulations interpreted by effective medium theory reveal that channel size impacts microscale properties of proton, water, and electrokinetic transport and with different functionality. Because there is a distribution of water-filled channel sizes in PFSA membranes, the corresponding distribution of microscale transport properties is different for each mode of transport, which impacts the aggregated macroscopic observables. Consequently, the transport pathways that water and protons travel through the membrane are not the same. Moreover, the distribution of properties induces local gradients of water chemical potential (and proton electrochemical potential) that act on proton (and water) transport through electrokinetic coupling. As a result, mesoscale effects, as characterized by the transport coefficient of tortuosity, lead to starkly different behavior for different types of transport. These effects are relatively long range and can create system-size-dependent behavior for experiments and simulations at the identified representative-elementary size of about 60 nm.

The methodology presented in this paper can be easily extended to modeling transport in other water-filled, ion-conductive membrane systems, such those with multiple cations and anion exchange membranes. To model systems with a different mobile ion, the only changes would be to the microscale transport properties and membrane channel properties (e.g., the mean channel size). To treat systems with multiple mobile ionic species, the model would also need to include ion-ion transport coefficients. The presence of multiple ions may introduce additional mesoscale effects such as how these species partition between small and large channels and the resulting impact on macroscale transport properties.^{21,91}

Supporting Information

Supporting information contains appendixes with derivations of the pedagogical model, the calculation of microscale transport coefficients, algorithm of network generation and solutions, and effective medium theory.

Acknowledgements

We would like to thank Jeff Gostick for his helpful discussions around openPNM and pore-network modeling. The initial model development was supported the Hydrogen and Fuel Cell Technologies Office (HFTO), Office of Energy Efficiency and Renewable Energy, US Department of Energy (DOE) through the Fuel Cell Performance and Durability (FC-PAD) and Million Mile Fuel Cell Truck (M2FCT) consortia under contract no. DE-AC02-05CH11231, and the model refinement and simulations were supported by the Army Research Office under contract AWD00004718.

References

- (1) Kreuer, K.-D.; Paddison, S. J.; Spohr, E.; Schuster, M. Transport in Proton Conductors for Fuel-Cell Applications: Simulations, Elementary Reactions, and Phenomenology. *Chem. Rev.* **2004**, *104* (10), 4637–4678. <https://doi.org/10.1021/cr020715f>.
- (2) Kusoglu, A.; Weber, A. Z. New Insights into Perfluorinated Sulfonic-Acid Ionomers. *Chem. Rev.* **2017**, *117* (3), 987–1104. <https://doi.org/10.1021/acs.chemrev.6b00159>.
- (3) Kushner, D. I.; Crothers, A. R.; Kusoglu, A.; Weber, A. Z. Transport Phenomena in Flow Battery Ion-Conducting Membranes. *Current Opinion in Electrochemistry* **2020**, *21*, 132–139. <https://doi.org/10.1016/j.coelec.2020.01.010>.
- (4) Adhikari, S.; Pagels, M. K.; Jeon, J. Y.; Bae, C. Ionomers for Electrochemical Energy Conversion & Storage Technologies. *Polymer* **2020**, *211*, 123080. <https://doi.org/10.1016/j.polymer.2020.123080>.
- (5) Fuller, T. F.; Newman, J. Experimental Determination of the Transport Number of Water in Nafion 117 Membrane. *J. Electrochem. Soc.* **1992**, *139* (5), 1332. <https://doi.org/10.1149/1.2069407>.
- (6) Weber, A. Z.; Newman, J. Transport in Polymer-Electrolyte Membranes : II. Mathematical Model. *J. Electrochem. Soc.* **2004**, *151* (2), A311. <https://doi.org/10.1149/1.1639157>.
- (7) Meyers, J. P.; Newman, J. Simulation of the Direct Methanol Fuel Cell : II. Modeling and Data Analysis of Transport and Kinetic Phenomena. *J. Electrochem. Soc.* **2002**, *149* (6), A718. <https://doi.org/10.1149/1.1473189>.
- (8) Weber, A. Z.; Borup, R. L.; Darling, R. M.; Das, P. K.; Dursch, T. J.; Gu, W.; Harvey, D.; Kusoglu, A.; Litster, S.; Mench, M. M.; Mukundan, R.; Owejan, J. P.; Pharoah, J. G.; Secanell, M.; Zenyuk, I. V. A Critical Review of Modeling Transport Phenomena in Polymer-Electrolyte Fuel Cells. *J. Electrochem. Soc.* **2014**, *161* (12), F1254. <https://doi.org/10.1149/2.0751412jes>.
- (9) Berrod, Q.; Lyonard, S.; Guillermo, A.; Ollivier, J.; Frick, B.; Manseri, A.; Améduri, B.; Gébel, G. Nanostructure and Transport Properties of Proton Conducting Self-Assembled Perfluorinated Surfactants: A Bottom-Up Approach toward PFSA Fuel Cell Membranes. *Macromolecules* **2015**, *48* (17), 6166–6176. <https://doi.org/10.1021/acs.macromol.5b00770>.
- (10) Hickner, M. A.; Pivovar, B. S. The Chemical and Structural Nature of Proton Exchange Membrane Fuel Cell Properties. *Fuel Cells* **2005**, *5* (2), 213–229. <https://doi.org/10.1002/fuce.200400064>.
- (11) Sasidhar, V.; Ruckenstein, E. Electrolyte Osmosis through Capillaries. *Journal of Colloid and Interface Science* **1981**, *82* (2), 439–457. [https://doi.org/10.1016/0021-9797\(81\)90386-6](https://doi.org/10.1016/0021-9797(81)90386-6).
- (12) Oren, Y. S.; Biesheuvel, P. M. Theory of Ion and Water Transport in Reverse-Osmosis Membranes. *Phys. Rev. Applied* **2018**, *9* (2), 024034. <https://doi.org/10.1103/PhysRevApplied.9.024034>.
- (13) Kamcev, J.; Paul, D. R.; Manning, G. S.; Freeman, B. D. Accounting for Frame of Reference and Thermodynamic Non-Idealities When Calculating Salt Diffusion Coefficients in Ion Exchange Membranes. *Journal of Membrane Science* **2017**, *537*, 396–406. <https://doi.org/10.1016/j.memsci.2017.05.034>.

- (14) Cwirko, E. H.; Carbonell, R. G. Ionic Equilibria in Ion-Exchange Membranes: A Comparison of Pore Model Predictions with Experimental Results. *Journal of Membrane Science* **1992**, *67* (2), 211–226. [https://doi.org/10.1016/0376-7388\(92\)80026-G](https://doi.org/10.1016/0376-7388(92)80026-G).
- (15) Yang, Y.; Pintauro, P. N. Multicomponent Space-Charge Transport Model for Ion-Exchange Membranes with Variable Pore Properties. *Ind. Eng. Chem. Res.* **2004**, *43* (12), 2957–2965. <https://doi.org/10.1021/ie030558q>.
- (16) Geise, G. M.; Paul, D. R.; Freeman, B. D. Fundamental Water and Salt Transport Properties of Polymeric Materials. *Progress in Polymer Science* **2014**, *39* (1), 1–42. <https://doi.org/10.1016/j.progpolymsci.2013.07.001>.
- (17) Thieu, L. M.; Zhu, L.; Korovich, A. G.; Hickner, M. A.; Madsen, L. A. Multiscale Tortuous Diffusion in Anion and Cation Exchange Membranes. *Macromolecules* **2019**, *52* (1), 24–35. <https://doi.org/10.1021/acs.macromol.8b02206>.
- (18) Koter, S.; Kujawski, W.; Koter, I. Transport of Electrolytes through Charged Membranes — on the Relations between the Independent Transport Coefficients. *Desalination* **2009**, *241* (1), 75–80. <https://doi.org/10.1016/j.desal.2008.01.058>.
- (19) Koter, S. Transport of Simple Electrolyte Solutions through Ion-Exchange Membranes—the Capillary Model. *Journal of Membrane Science* **2002**, *206* (1), 201–215. [https://doi.org/10.1016/S0376-7388\(01\)00763-3](https://doi.org/10.1016/S0376-7388(01)00763-3).
- (20) Zhang, R.; Chen, Y.; Troya, D.; Madsen, L. A. Relating Geometric Nanoconfinement and Local Molecular Environment to Diffusion in Ionic Polymer Membranes. *Macromolecules* **2020**, *53* (9), 3296–3305. <https://doi.org/10.1021/acs.macromol.9b02755>.
- (21) Crothers, A. R.; Darling, R. M.; Kusoglu, A.; Radke, C. J.; Weber, A. Z. Theory of Multicomponent Phenomena in Cation-Exchange Membranes: Part II. Transport Model and Validation. *J. Electrochem. Soc.* **2020**, *167* (1), 013548. <https://doi.org/10.1149/1945-7111/ab6724>.
- (22) Cwirko, E. H.; Carbonell, R. G. Interpretation of Transport Coefficients in Nafion Using a Parallel Pore Model. *Journal of Membrane Science* **1992**, *67* (2), 227–247. [https://doi.org/10.1016/0376-7388\(92\)80027-H](https://doi.org/10.1016/0376-7388(92)80027-H).
- (23) Dullien, F. A. L. *Single-Phase Transport Phenomena in Porous Media*; Academic Press, 1992; pp 237–317. <https://doi.org/10.1016/B978-0-12-223651-8.50009-2>.
- (24) Mackie, J. S.; Meares, P.; Rideal, E. K. The Diffusion of Electrolytes in a Cation-Exchange Resin Membrane I. Theoretical. *Proceedings of the Royal Society of London. Series A. Mathematical and Physical Sciences* **1955**, *232* (1191), 498–509. <https://doi.org/10.1098/rspa.1955.0234>.
- (25) Wesselingh, J. A.; Vonk, P.; Kraaijeveld, G. Exploring the Maxwell-Stefan Description of Ion Exchange. *The Chemical Engineering Journal and the Biochemical Engineering Journal* **1995**, *57* (2), 75–89. [https://doi.org/10.1016/0923-0467\(94\)02932-6](https://doi.org/10.1016/0923-0467(94)02932-6).
- (26) Amsden, B. Solute Diffusion within Hydrogels. Mechanisms and Models. *Macromolecules* **1998**, *31* (23), 8382–8395. <https://doi.org/10.1021/ma980765f>.
- (27) Schultz, S. G. *Basic Principles of Membrane Transport*; IUPAB biophysics series; Cambridge University Press: Cambridge [Eng.]; New York, 1980.
- (28) Diederichsen, K. M.; Brow, R. R.; Stoykovich, M. P. Percolating Transport and the Conductive Scaling Relationship in Lamellar Block Copolymers under Confinement. *ACS Nano* **2015**, *9* (3), 2465–2476. <https://doi.org/10.1021/acs.nano.5b01321>.

- (29) Galluzzo, M. D.; Loo, W. S.; Wang, A. A.; Walton, A.; Maslyn, J. A.; Balsara, N. P. Measurement of Three Transport Coefficients and the Thermodynamic Factor in Block Copolymer Electrolytes with Different Morphologies. *J. Phys. Chem. B* **2020**, *124* (5), 921–935. <https://doi.org/10.1021/acs.jpccb.9b11066>.
- (30) Yaroshchuk, A. E. Osmosis and Reverse Osmosis in Fine-Porous Charged Diaphragms and Membranes. *Advances in Colloid and Interface Science* **1995**, *60* (1), 1–93. [https://doi.org/10.1016/0001-8686\(95\)00246-M](https://doi.org/10.1016/0001-8686(95)00246-M).
- (31) Pintauro, P. N.; Bennion, D. N. Mass Transport of Electrolytes in Membranes. 1. Development of Mathematical Transport Model. *Ind. Eng. Chem. Fund.* **1984**, *23* (2), 230–234. <https://doi.org/10.1021/i100014a016>.
- (32) Bird, R. B.; Stewart, W. E.; Lightfoot, E. N. *Transport Phenomena*, Rev. 2. ed.; Wiley: New York, 2007.
- (33) Fuller, T. F. Solid-Polymer-Electrolyte Fuel Cells. Ph.D., University of California, Berkeley, United States -- California, 1992.
- (34) Groot, S. R. de; Mazur, P. *Non-Equilibrium Thermodynamics*, Dover ed.; Dover Publications: New York, 1984.
- (35) Newman, J. S.; Thomas-Alyea, K. E. *Electrochemical Systems*, 3rd ed.; J. Wiley: Hoboken, N.J, 2004.
- (36) Alizadeh, S.; Bazant, M. Z.; Mani, A. Impact of Network Heterogeneity on Electrokinetic Transport in Porous Media. *Journal of Colloid and Interface Science* **2019**, *553*, 451–464. <https://doi.org/10.1016/j.jcis.2019.06.023>.
- (37) Alizadeh, S.; Mani, A. Multiscale Model for Electrokinetic Transport in Networks of Pores, Part I: Model Derivation. *Langmuir* **2017**, *33* (25), 6205–6219. <https://doi.org/10.1021/acs.langmuir.6b03816>.
- (38) Obliger, A.; Jardat, M.; Coelho, D.; Bekri, S.; Rotenberg, B. Pore Network Model of Electrokinetic Transport Through Charged Porous Media. *Phys. Rev. E* **2014**, *89* (4), 043013. <https://doi.org/10.1103/PhysRevE.89.043013>.
- (39) Eikerling, M.; Kornyshev, A. A.; Kuznetsov, A. M.; Ulstrup, J.; Walbran, S. Mechanisms of Proton Conductance in Polymer Electrolyte Membranes. *J. Phys. Chem. B* **2001**, *105* (17), 3646–3662. <https://doi.org/10.1021/jp003182s>.
- (40) Gostick, J. T.; Weber, A. Z. Resistor-Network Modeling of Ionic Conduction in Polymer Electrolytes. *Electrochimica Acta* **2015**, *179*, 137–145. <https://doi.org/10.1016/j.electacta.2015.03.126>.
- (41) Hwang, G. S.; Kaviani, M.; Gostick, J. T.; Kientz, B.; Weber, A. Z.; Kim, M. H. Role of Water States on Water Uptake and Proton Transport in Nafion Using Molecular Simulations and Bimodal Network. *Polymer* **2011**, *52* (12), 2584–2593. <https://doi.org/10.1016/j.polymer.2011.03.056>.
- (42) Berg, P.; Stornes, M. Towards a Consistent Interpretation of Electro-Osmotic Drag in Polymer Electrolyte Membranes. *Fuel Cells* **2016**, *16* (6), 715–724. <https://doi.org/10.1002/fuce.201500210>.
- (43) Kreuer, K.-D.; Portale, G. A Critical Revision of the Nano-Morphology of Proton Conducting Ionomers and Polyelectrolytes for Fuel Cell Applications. *Advanced Functional Materials* **2013**, *23* (43), 5390–5397. <https://doi.org/10.1002/adfm.201300376>.

- (44) *nafion membrane, chemours nafion, proton exchange membrane*. Chemours.
<https://www.nafion.com:443/en/products/sulfonic-membranes> (accessed 2020-10-22).
- (45) Allen, F. I.; Comolli, L. R.; Kusoglu, A.; Modestino, M. A.; Minor, A. M.; Weber, A. Z. Morphology of Hydrated As-Cast Nafion Revealed through Cryo Electron Tomography. *ACS Macro Lett.* **2015**, *4* (1), 1–5. <https://doi.org/10.1021/mz500606h>.
- (46) Crothers, A. R.; Radke, C. J.; Weber, A. Z. Multiscale Model of Proton Transport in Perfluorosulfonic-Acid Membrane. *ECS Trans.* **2015**, *69* (17), 731.
<https://doi.org/10.1149/06917.0731ecst>.
- (47) Savage, J.; Voth, G. A. Proton Solvation and Transport in Realistic Proton Exchange Membrane Morphologies. *J. Phys. Chem. C* **2016**, *120* (6), 3176–3186.
<https://doi.org/10.1021/acs.jpcc.5b11168>.
- (48) Savage, J.; Voth, G. A. Persistent Subdiffusive Proton Transport in Perfluorosulfonic Acid Membranes. *J. Phys. Chem. Lett.* **2014**, *5* (17), 3037–3042.
<https://doi.org/10.1021/jz5014467>.
- (49) Duin, A. C. T. van; Zou, C.; Joshi, K.; Bryantsev, V.; Goddard, W. A. CHAPTER 6:A Reaxff Reactive Force-Field for Proton Transfer Reactions in Bulk Water and Its Applications to Heterogeneous Catalysis. In *Computational Catalysis*; 2013; pp 223–243.
<https://doi.org/10.1039/9781849734905-00223>.
- (50) Schmitt, U. W.; Voth, G. A. The Computer Simulation of Proton Transport in Water. *J. Chem. Phys.* **1999**, *111* (20), 9361–9381. <https://doi.org/10.1063/1.480032>.
- (51) Wang, C.; Clark, J. K.; Kumar, M.; Paddison, S. J. An Ab Initio Study of the Primary Hydration and Proton Transfer of CF₃SO₃H and CF₃O(CF₂)₂SO₃H: Effects of the Hybrid Functional and Inclusion of Diffuse Functions. *Solid State Ionics* **2011**, *199–200*, 6–13.
<https://doi.org/10.1016/j.ssi.2011.07.002>.
- (52) Karo, J.; Aabloo, A.; Thomas, J. O.; Brandell, D. Molecular Dynamics Modeling of Proton Transport in Nafion and Hyflon Nanostructures. *J. Phys. Chem. B* **2010**, *114* (18), 6056–6064. <https://doi.org/10.1021/jp903288y>.
- (53) Tse, Y.-L. S.; Herring, A. M.; Kim, K.; Voth, G. A. Molecular Dynamics Simulations of Proton Transport in 3M and Nafion Perfluorosulfonic Acid Membranes. *J. Phys. Chem. C* **2013**, *117* (16), 8079–8091. <https://doi.org/10.1021/jp400693g>.
- (54) Chapman, T. W. The Transport Properties of Concentrated Electrolytic Solutions. Ph.D., University of California, Berkeley, United States -- California, 1967.
- (55) Bockris, J. O.; Reddy, A. K. N. *Volume 1: Modern Electrochemistry: Ionics*, 2nd ed.; Bockris, J. O., Ed.; Springer US, 1998. <https://doi.org/10.1007/b114546>.
- (56) Devanathan, R.; Idupulapati, N.; Baer, M. D.; Mundy, C. J.; Dupuis, M. Ab Initio Molecular Dynamics Simulation of Proton Hopping in a Model Polymer Membrane. *J. Phys. Chem. B* **2013**, *117* (51), 16522–16529. <https://doi.org/10.1021/jp410229u>.
- (57) Devanathan, R.; Venkatnathan, A.; Dupuis, M. Atomistic Simulation of Nafion Membrane: I. Effect of Hydration on Membrane Nanostructure. *J. Phys. Chem. B* **2007**, *111* (28), 8069–8079. <https://doi.org/10.1021/jp0726992>.
- (58) DeGroot, M. H.; Schervish, M. J. *Probability and Statistics*, 4th ed.; Addison-Wesley: Boston, 2012.

- (59) Monteiro, M. J. Fitting Molecular Weight Distributions Using a Log-Normal Distribution Model. *European Polymer Journal* **2015**, *65*, 197–201. <https://doi.org/10.1016/j.eurpolymj.2015.01.009>.
- (60) Brent, R. P. *Algorithms for Minimization without Derivatives*; Dover Publications: Mineola, N.Y., 2002.
- (61) Su, G. M.; Cordova, I. A.; Yandrasits, M. A.; Lindell, M.; Feng, J.; Wang, C.; Kusoglu, A. Chemical and Morphological Origins of Improved Ion Conductivity in Perfluoro Ionene Chain Extended Ionomers. *J. Am. Chem. Soc.* **2019**, *141* (34), 13547–13561. <https://doi.org/10.1021/jacs.9b05322>.
- (62) Loupe, N.; Abu-Hakmeh, K.; Gao, S.; Gonzalez, L.; Ingargiola, M.; Mathiowetz, K.; Cruse, R.; Doan, J.; Schide, A.; Salas, I.; Dimakis, N.; Jang, S. S.; Goddard, W. A.; Smotkin, E. S. Group Vibrational Mode Assignments as a Broadly Applicable Tool for Characterizing Ionomer Membrane Structure as a Function of Degree of Hydration. *Chem. Mater.* **2020**, *32* (5), 1828–1843. <https://doi.org/10.1021/acs.chemmater.9b04037>.
- (63) Moukheiber, E.; De Moor, G.; Flandin, L.; Bas, C. Investigation of Ionomer Structure through Its Dependence on Ion Exchange Capacity (IEC). *Journal of Membrane Science* **2012**, *389*, 294–304. <https://doi.org/10.1016/j.memsci.2011.10.041>.
- (64) Delacourt, C.; Newman, J. Mathematical Modeling of a Cation-Exchange Membrane Containing Two Cations. *J. Electrochem. Soc.* **2008**, *155* (11), B1210. <https://doi.org/10.1149/1.2977960>.
- (65) Kreuer, K. D.; Schuster, M.; Obliers, B.; Diat, O.; Traub, U.; Fuchs, A.; Klock, U.; Paddison, S. J.; Maier, J. Short-Side-Chain Proton Conducting Perfluorosulfonic Acid Ionomers: Why They Perform Better in PEM Fuel Cells. *Journal of Power Sources* **2008**, *178* (2), 499–509. <https://doi.org/10.1016/j.jpowsour.2007.11.011>.
- (66) Kusoglu, A.; Dursch, T. J.; Weber, A. Z. Nanostructure/Swelling Relationships of Bulk and Thin-Film PFSA Ionomers. *Advanced Functional Materials* **2016**, *26* (27), 4961–4975. <https://doi.org/10.1002/adfm.201600861>.
- (67) Edmondson, C. A.; Fontanella, J. J. Free Volume and Percolation in S-SEBS and Fluorocarbon Proton Conducting Membranes. *Solid State Ionics* **2002**, *152–153*, 355–361. [https://doi.org/10.1016/S0167-2738\(02\)00336-3](https://doi.org/10.1016/S0167-2738(02)00336-3).
- (68) Zawodzinski, T. A.; Springer, T. E.; Uribe, F.; Gottesfeld, S. Characterization of Polymer Electrolytes for Fuel Cell Applications. *Solid State Ionics* **1993**, *60* (1), 199–211. [https://doi.org/10.1016/0167-2738\(93\)90295-E](https://doi.org/10.1016/0167-2738(93)90295-E).
- (69) Zawodzinski, T. A.; Derouin, C.; Radzinski, S.; Sherman, R. J.; Smith, V. T.; Springer, T. E.; Gottesfeld, S. Water Uptake by and Transport Through Nafion® 117 Membranes. *J. Electrochem. Soc.* **1993**, *140* (4), 1041. <https://doi.org/10.1149/1.2056194>.
- (70) Maldonado, L.; Perrin, J.-C.; Dillet, J.; Lottin, O. Characterization of Polymer Electrolyte Nafion Membranes: Influence of Temperature, Heat Treatment and Drying Protocol on Sorption and Transport Properties. *Journal of Membrane Science* **2012**, *389*, 43–56. <https://doi.org/10.1016/j.memsci.2011.10.014>.
- (71) Ochi, S.; Kamishima, O.; Mizusaki, J.; Kawamura, J. Investigation of Proton Diffusion in Nafion®117 Membrane by Electrical Conductivity and NMR. *Solid State Ionics* **2009**, *180* (6), 580–584. <https://doi.org/10.1016/j.ssi.2008.12.035>.

- (72) Sone, Y.; Ekdunge, P.; Simonsson, D. Proton Conductivity of Nafion 117 as Measured by a Four-Electrode AC Impedance Method. *J. Electrochem. Soc.* **1996**, *143* (4), 1254. <https://doi.org/10.1149/1.1836625>.
- (73) Shi, S.; Dursch, T. J.; Blake, C.; Mukundan, R.; Borup, R. L.; Weber, A. Z.; Kusoglu, A. Impact of Hygrothermal Aging on Structure/Function Relationship of Perfluorosulfonic-Acid Membrane. *Journal of Polymer Science Part B: Polymer Physics* **2016**, *54* (5), 570–581. <https://doi.org/10.1002/polb.23946>.
- (74) Shi, S.; Weber, A. Z.; Kusoglu, A. Structure-Transport Relationship of Perfluorosulfonic-Acid Membranes in Different Cationic Forms. *Electrochimica Acta* **2016**, *220*, 517–528. <https://doi.org/10.1016/j.electacta.2016.10.096>.
- (75) Peron, J.; Mani, A.; Zhao, X.; Edwards, D.; Adachi, M.; Soboleva, T.; Shi, Z.; Xie, Z.; Navessin, T.; Holdcroft, S. Properties of Nafion® NR-211 Membranes for PEMFCs. *Journal of Membrane Science* **2010**, *356* (1), 44–51. <https://doi.org/10.1016/j.memsci.2010.03.025>.
- (76) Luo, Z.; Chang, Z.; Zhang, Y.; Liu, Z.; Li, J. Electro-Osmotic Drag Coefficient and Proton Conductivity in Nafion® Membrane for PEMFC. *International Journal of Hydrogen Energy* **2010**, *35* (7), 3120–3124. <https://doi.org/10.1016/j.ijhydene.2009.09.013>.
- (77) Ise, M.; Kreuer, K. D.; Maier, J. Electroosmotic Drag in Polymer Electrolyte Membranes: An Electrophoretic NMR Study. *Solid State Ionics* **1999**, *125* (1), 213–223. [https://doi.org/10.1016/S0167-2738\(99\)00178-2](https://doi.org/10.1016/S0167-2738(99)00178-2).
- (78) Ge, S.; Yi, B.; Ming, P. Experimental Determination of Electro-Osmotic Drag Coefficient in Nafion Membrane for Fuel Cells. *J. Electrochem. Soc.* **2006**, *153* (8), A1443. <https://doi.org/10.1149/1.2203934>.
- (79) Xu, F.; Leclerc, S.; Stemmelen, D.; Perrin, J.-C.; Retournard, A.; Canet, D. Study of Electro-Osmotic Drag Coefficients in Nafion Membrane in Acid, Sodium and Potassium Forms by Electrophoresis NMR. *Journal of Membrane Science* **2017**, *536*, 116–122. <https://doi.org/10.1016/j.memsci.2017.04.067>.
- (80) Edmondson, C. A.; Fontanella, J. J.; Chung, S. H.; Greenbaum, S. G.; Wnek, G. E. Complex Impedance Studies of S-SEBS Block Polymer Proton-Conducting Membranes. *Electrochimica Acta* **2001**, *46* (10), 1623–1628. [https://doi.org/10.1016/S0013-4686\(00\)00762-3](https://doi.org/10.1016/S0013-4686(00)00762-3).
- (81) Gong, X.; Bandis, A.; Tao, A.; Meresi, G.; Wang, Y.; Inglefield, P. T.; Jones, A. A.; Wen, W.-Y. Self-Diffusion of Water, Ethanol and Decafluoropentane in Perfluorosulfonate Ionomer by Pulse Field Gradient NMR. *Polymer* **2001**, *42* (15), 6485–6492. [https://doi.org/10.1016/S0032-3861\(01\)00119-7](https://doi.org/10.1016/S0032-3861(01)00119-7).
- (82) Ma, Z.; Jiang, R.; Myers, M. E.; Thompson, E. L.; Gittleman, C. S. NMR Studies of Proton Transport in Fuel Cell Membranes at Sub-Freezing Conditions. *J. Mater. Chem.* **2011**, *21* (25), 9302–9311. <https://doi.org/10.1039/C1JM10097A>.
- (83) Tsushima, S.; Teranishi, K.; Hirai, S. Water Diffusion Measurement in Fuel-Cell SPE Membrane by NMR. *Energy* **2005**, *30* (2), 235–245. <https://doi.org/10.1016/j.energy.2004.04.013>.
- (84) Zawodzinski, T. A.; Neeman, M.; Sillerud, L. O.; Gottesfeld, S. Determination of Water Diffusion Coefficients in Perfluorosulfonate Ionomeric Membranes. *J. Phys. Chem.* **1991**, *95* (15), 6040–6044. <https://doi.org/10.1021/j100168a060>.

- (85) Okada, T.; Satou, H.; Okuno, M.; Yuasa, M. Ion and Water Transport Characteristics of Perfluorosulfonated Ionomer Membranes with H⁺ and Alkali Metal Cations. *J. Phys. Chem. B* **2002**, *106* (6), 1267–1273. <https://doi.org/10.1021/jp013195l>.
- (86) Crothers, A. R.; Radke, C. J.; Weber, A. Z. Impact of Nano- and Mesoscales on Macroscopic Cation Conductivity in Perfluorinated-Sulfonic-Acid Membranes. *J. Phys. Chem. C* **2017**, *121* (51), 28262–28274. <https://doi.org/10.1021/acs.jpcc.7b07360>.
- (87) Kirkpatrick, S. Percolation and Conduction. *Rev. Mod. Phys.* **1973**, *45* (4), 574–588. <https://doi.org/10.1103/RevModPhys.45.574>.
- (88) Bonilla, M. R.; Bhatia, S. K. Multicomponent Effective Medium–Correlated Random Walk Theory for the Diffusion of Fluid Mixtures through Porous Media. *Langmuir* **2012**, *28* (1), 517–533. <https://doi.org/10.1021/la2040888>.
- (89) Tesfaye, M.; Kushner, D. I.; McCloskey, B. D.; Weber, A. Z.; Kusoglu, A. Thermal Transitions in Perfluorosulfonated Ionomer Thin-Films. *ACS Macro Lett.* **2018**, *7* (10), 1237–1242. <https://doi.org/10.1021/acsmacrolett.8b00628>.
- (90) Tesfaye, M.; Kushner, D. I.; Kusoglu, A. Interplay between Swelling Kinetics and Nanostructure in Perfluorosulfonic Acid Thin-Films: Role of Hygrothermal Aging. *ACS Appl. Polym. Mater.* **2019**, *1* (4), 631–635. <https://doi.org/10.1021/acsapm.9b00005>.
- (91) Crothers, A. R.; Darling, R. M.; Kusoglu, A.; Radke, C. J.; Weber, A. Z. Theory of Multicomponent Phenomena in Cation-Exchange Membranes: Part I. Thermodynamic Model and Validation. *J. Electrochem. Soc.* **2020**, *167* (1), 013547. <https://doi.org/10.1149/1945-7111/ab6723>.

Graphical Abstract

